ARTICLES
https://doi.org/10.1038/s41929-021-00703-0

nature catalysis

In-situ reconstructed Ru atom array on α-MnO_2 with enhanced performance for acidic water oxidation

Chao Lin[1,2,6], Ji-Li Li[3,6], Xiaopeng Li[1]✉, Shuai Yang[4], Wei Luo[1], Yaojia Zhang[1], Sung-Hae Kim[2], Dong-Hyung Kim[2], Sambhaji S. Shinde[2], Ye-Fei Li[3], Zhi-Pan Liu[3]✉, Zheng Jiang[4,5]✉ and Jung-Ho Lee[2]✉

The development of acid-stable oxygen evolution reaction electrocatalysts is essential for high-performance water splitting. Here, we report an electrocatalyst with Ru-atom-array patches supported on α-MnO_2 (Ru/MnO_2) for the oxygen evolution reaction following a mechanism that involves only *O and *OH species as intermediates. This mechanism allows direct O–O radical coupling for O_2 evolution. Ru/MnO_2 shows high activity (161 mV at 10 mA cm^{-2}) and outstanding stability with small degradation after 200 h operation, making it one of the best-performing acid-stable oxygen evolution reaction catalysts. Operando vibrational and mass spectroscopy measurements were performed to probe the reaction intermediates and gaseous products for validating the oxygen evolution reaction pathway. First-principles calculations confirmed the cooperative catalysis mechanism with a reduced energy barrier. Time-dependent elemental analysis demonstrated the occurrence of the in-situ dynamic cation exchange reaction during the oxygen evolution reaction, which is the key for triggering the reconstruction of Ru atoms into the ordered array with high durability.

The prospect of a hydrogen economy offers the promise of decarbonizing energy sectors. Water splitting, which produces abundant renewable electricity, is regarded as an ideal route for producing hydrogen. The alkaline water electrolyser and proton exchange membrane water electrolyser (PEMWE) are two mainstream technologies that are used in the production of hydrogen. The PEMWE has attracted interest worldwide because it delivers purer H_2 with a greater current density and a higher energy efficiency than the alkaline water electrolyser[1–3]. However, the strong acidic operation conditions in commercial PEMWEs requires the use of precious metals such as platinum (US\$36,084 kg^{-1})[4] and iridium (US\$60,670 kg^{-1})[4] as electrocatalysts for the hydrogen evolution reaction (HER) and oxygen evolution reaction (OER) at the cathode and anode, which restricts the global deployment of this technology. The OER is a four proton-coupled electron transfer electrochemical reaction that displays a higher reaction energy barrier than the HER, which involves two proton–electron transfers. The loading of Ir (1–3 mg cm^{-2}) required at the anode is therefore more than five times greater than that of Pt (approximately 0.2 mg cm^{-2}) at the cathode in state-of-the-art PEMWEs. Ru might be a potential candidate for the replacement of Ir because of its higher earth abundance (US\$9,523 kg^{-1})[4]. In addition, RuO_2 usually shows better OER activity than IrO_2 (refs. [5,6]). However, the inferior dissolution resistance of Ru oxides in acidic anodization conditions imposes a challenge to the development of high-performance Ru-based OER electrocatalysts[7].

According to the widely accepted conventional adsorbate evolution mechanism (AEM), the OER involves multiple oxygen reaction intermediates such as *OH, *O and *OOH, as displayed in Fig. 1a (refs. [8,9]). The binding energies of the intermediates are linearly correlated and follow the scaling relationship $\Delta G_{OOH} = \Delta G_{OH} + 3.2 \pm 0.2$ eV (ref. [10]). The binding energy of each intermediate cannot be independently modulated, and a high overpotential (η) therefore is still required to drive the reaction, with a calculated theoretical limit of approximately 370 ± 100 mV (refs. [11,12]). However, some recently reported electrocatalysts possess OER activity that is better than the theoretical limit[13–18], implying the presence of other reaction mechanisms. A lattice-oxygen-mediated mechanism[19,20] (LOM) has been proposed as an alternative route; moreover, the oxide path mechanism[21,22] (OPM) for heterogeneous catalysts or the oxo–oxo coupling mechanism[23] for homogeneous catalysts is more recommendable for further improving OER performance. LOM includes the participation of activated lattice oxygen in the OER, facilitating O–O coupling (Fig. 1b). However, the generated oxygen vacancy defects cause the metal species to detach from the catalyst surface, leading to the rapid degradation of the electrocatalysts. This process can explain why electrochemically synthesized (defect-rich) RuO_2 (refs. [24,25]) produces a higher dissolution rate than thermally prepared RuO_2 (ref. [26]). In contrast to AEM and LOM, OPM is more ideal for designing high-performance OER electrocatalysts, since this mechanism allows direct O–O radical coupling without the generation of oxygen vacancy defects and extra reaction

---

[1]State Key Laboratory for Modification of Chemical Fibers and Polymer Materials, College of Materials Science and Engineering, Donghua University, Songjiang District, Shanghai, P. R. China. [2]Department of Materials Science and Chemical Engineering, Hanyang University, Ansan, Korea. [3]Collaborative Innovation Center of Chemistry for Energy Material, Key Laboratory of Computational Physical Science (Ministry of Education), Shanghai Key Laboratory of Molecular Catalysis and Innovative Materials, Department of Chemistry, Fudan University, Shanghai, P. R. China. [4]Shanghai Synchrotron Radiation Facility, Shanghai Advanced Research Institute, Chinese Academy of Sciences, Shanghai, P. R. China. [5]Shanghai Institute of Applied Physics, Chinese Academy of Science, Shanghai, P. R. China. [6]These authors contributed equally: Chao Lin, Ji-Li Li. ✉e-mail: xiaopeng.li@dhu.edu.cn; zpliu@fudan.edu.cn; jiangzheng@sinap.ac.cn; jungho@hanyang.ac.kr

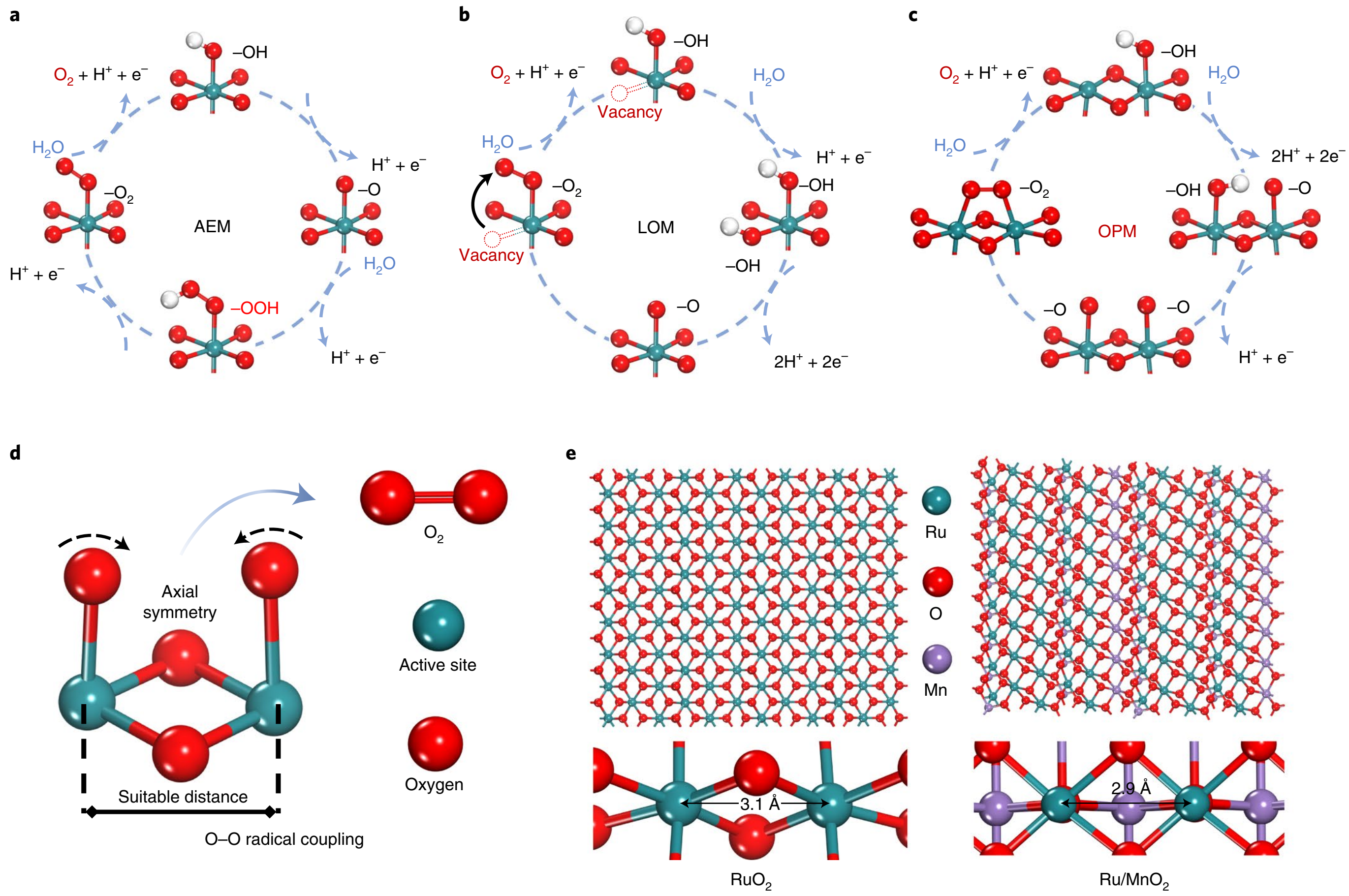

Fig. 1 | Schematics of OER mechanisms for a heterogeneous Ru-based OER electrocatalyst. Schematic illustration of simplified OER mechanisms. **a**, The AEM. **b**, The LOM. **c**, The OPM. **d**, O–O radical coupling promoted by symmetric dual active sites. **e**, Crystalline structure models of RuO_2 and α-MnO_2 with Ru atoms substituting for the Mn at surface sites.

intermediates (such as *OOH). Only *O and *OH act as OER intermediates under this mechanism (Fig. 1c). More importantly, the suitably located active metal sites work cooperatively to dissociate water and trigger *O radical coupling to produce O_2 without the participation of the lattice oxygen. Ideally, heterogeneous electrocatalysts that are dominated by the OPM can break the scaling relationship without sacrificing stability. However, in contrast to the AEM and LOM, the OPM has more stringent requirements for the geometric configuration of metal active sites[27,28]. Symmetric dual-metal sites with appropriate atomic distances are expected to be advantageous in promoting O–O radical coupling with a low energy barrier (Fig. 1d). The first Fe-based OER catalyst that enables intramolecular O–O bond formation was reported by Masaoka and coworkers using a homogeneous iron complex with two adjacent penta-coordinated iron ions as active sites[28]. The following research proves that heterogeneous catalysts with similar active site design can work well in alkaline electrolyte[22]. However, to the best of our knowledge, such a design principle has never been applied to the fabrication of an acid-stable heterogeneous water oxidation electrocatalyst.

Herein, we report a crystalline α-MnO_2 nanofibre-supported Ru electrocatalyst (Ru/MnO_2) that satisfies the OPM design rule. The catalyst preparation was based on a one-step cation exchange method with Ru atoms substituting for surface Mn atoms. The positions of the Ru atoms therefore follow the periodic arrangement of the Mn sites in the crystalline α-MnO_2, resulting in the formation of small, regularly arranged Ru ensembles (for example, atom chains). The cation exchange reaction also occurs in situ during the OER, which not only triggers the reconstruction of the small Ru ensembles into large patches of Ru atom arrays, but also avoids metal-leaching-induced deactivation of the catalyst. The Ru atom array consists of symmetric Ru sites that are highly favourable for OPM-type OER. The interatomic Ru–Ru distance in Ru/MnO_2 (2.9 Å) is shorter than that in RuO_2 (3.1 Å), facilitating O–O radical coupling (Fig. 1e). Ru/MnO_2 with a Ru loading of 11.6 wt% (12Ru/MnO_2) delivers a small overpotential of only 161 mV at a current density of $10\,mA\,cm^{-2}$ ($\eta_{10} = 161\,mV$) and outstanding long-term durability (>200 h), making it one of the best-performing acid-stable OER catalysts. Extensive ex-situ and operando measurements that have probed the characteristic changes in the reaction intermediates and surface chemistry of Ru/MnO_2 indicate that the OER follows the OPM mechanism without the formation of *OOH. First-principles calculations confirm that when Ru/MnO_2 is used as a water oxidation electrocatalyst, the OER proceeds favourably via the OPM mechanism, while the conventional AEM mechanism has a higher energy barrier.

Results

Regularly arranged Ru atoms supported by MnO_2. The synthesis of crystalline α-MnO_2 was based on previously reported hydrothermal methods[29], in which scanning electron microscopy (SEM) revealed the nanofibre morphology (Supplementary Fig. 1a). The as-prepared α-MnO_2 was then transferred into an aqueous $RuCl_3$ solution for the cation exchange reaction (Supplementary Fig. 2

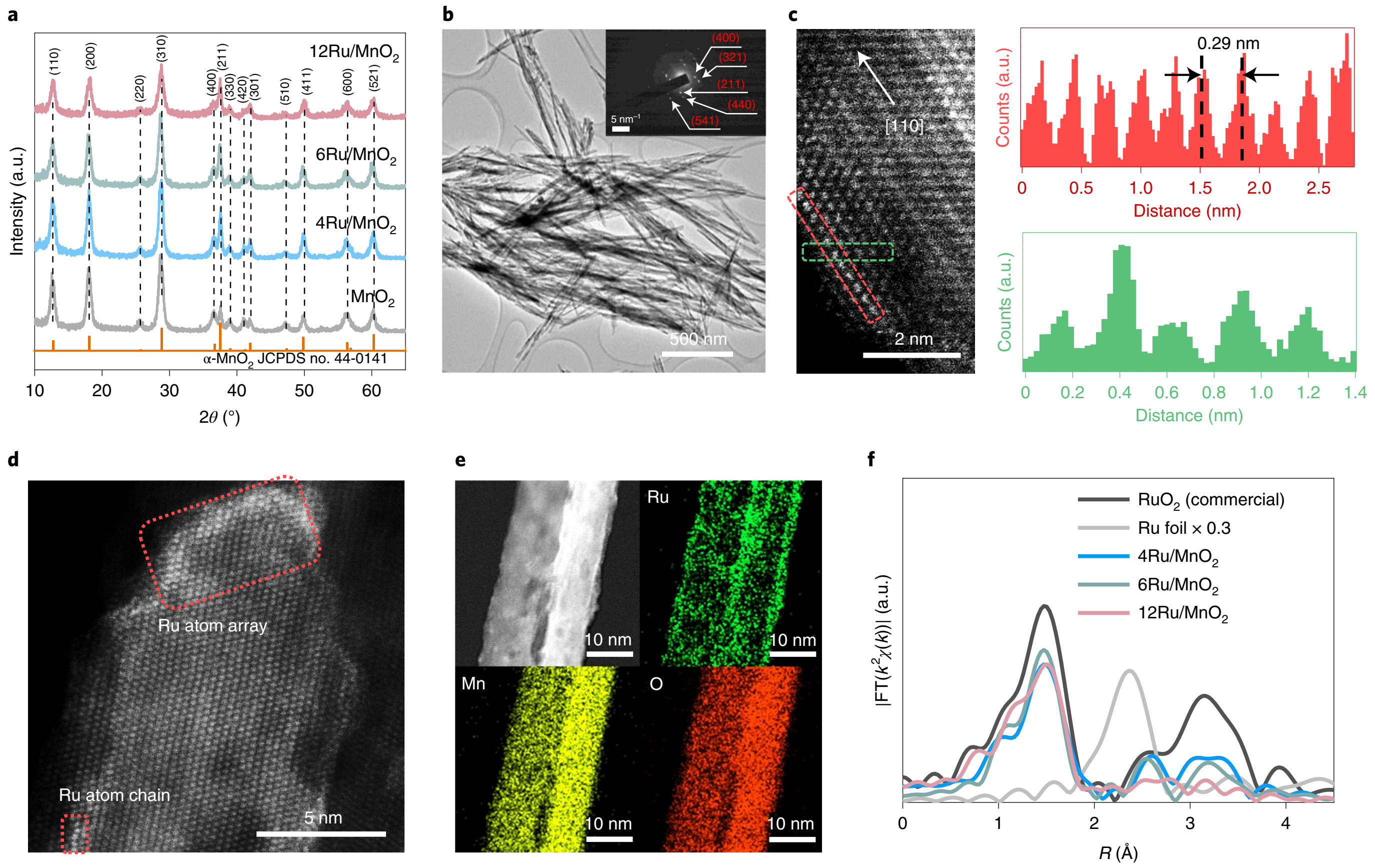

Fig. 2 | Structural characterization of the 12Ru/MnO$_2$ catalyst. a, X-ray diffraction patterns of MnO$_2$ and Ru/MnO$_2$ catalysts. **b**, TEM image of the 12Ru/MnO$_2$ catalyst. Inset, the corresponding selected area electron diffraction pattern. **c**, Aberration-corrected HAADF-STEM images of the 12Ru/MnO$_2$ catalyst. Insets to the right show the corresponding intensity profiles labelled with the red and green dashed boxes. **d**, Aberration-corrected HAADF-STEM image of the 12Ru/MnO$_2$ catalyst. The red dashed boxes highlight the presence of Ru atom chains or arrays. **e**, EDS mapping images of the 12Ru/MnO$_2$ catalyst. **f**, FT-EXAFS spectra for the Ru K edge of 4Ru/MnO$_2$, 6Ru/MnO$_2$, 12Ru/MnO$_2$, Ru foil and RuO$_2$. The *x* and *y* axes denote the radial distance and the Fourier transform of k^2-weighted EXAFS signals, respectively. a.u., arbitrary units.

and Supplementary Note 1)[30]. The loading of Ru was controlled by varying the concentration of RuCl$_3$. Three Ru/MnO$_2$ samples were obtained with Ru mass loadings of 3.8, 5.8 and 11.6 wt% as determined by inductively coupled plasma optical emission spectroscopy (ICP-OES). The samples are denoted as xRu/MnO$_2$ ($x = 4$, 6 and 12) in which x displays the weight percent of Ru loading. The concentrations of Mn and Ru ions in the supernatant were also measured after the cation exchange reaction using ICP-OES (Supplementary Table 1). The leaching of Mn ions accompanied with Ru deposition were observed, validating the occurrence of the cation exchange reaction. X-ray diffraction patterns of the 4, 6 and 12Ru/MnO$_2$ samples (Fig. 2a) matched the standard pattern of hollandite α-MnO$_2$ (ref. [31]; JCPDS file no. 44-0141), and no Ru-related peaks were detected, indicating a high Ru dispersion. SEM and transmission electron microscopy (TEM) characterizations showed that the morphology of the nanofibre remained unchanged following the cation exchange (Fig. 2b and Supplementary Figs. 1 and 3). Aberration-corrected high-angle annular dark-field scanning transmission electron microscopy (HAADF-STEM) was used to image the atomic structure of the 12Ru/MnO$_2$. The HAADF signal intensity is proportional to the square of the atomic number. Thus, the atomic columns containing Ru atoms are brighter than the neighbouring ones consisting of sole Mn atoms, whereas the lighter O atoms are not observable. The evenly spaced bright dots form a regular arrangement in the 12Ru/MnO$_2$ (Fig. 2c), which is identical to the periodic arrangement of the Mn sites in α-MnO$_2$. HAADF signal analysis reveals the interatomic distance of 2.9 Å (inset in Fig. 2c) for Ru–Ru ($d_{\text{Ru–Ru}}$), which matches the theoretical interatomic distance of Mn–Mn (2.9 Å). Ru atom chains and atom arrays were frequently observed during STEM characterization (Fig. 2c,d and Supplementary Fig. 4a–m), and irregular RuO$_x$ nanoclusters with a thickness of several atomic layers were also observed (Supplementary Fig. 4n–q). Energy dispersive spectroscopy (EDS) mapping confirmed the high dispersion of Ru, with locally intensified signals corresponding to Ru ensembles (Fig. 2e).

The local bonding environment of the Ru species was probed by extended X-ray absorption fine structure (EXAFS). Figure 2f shows the Fourier transform (FT) of the EXAFS spectrum of the Ru/MnO$_2$ catalysts, Ru foil and RuO$_2$. The FT-EXAFS profiles of the Ru/MnO$_2$ catalysts show a prominent peak at 1.47 Å that corresponds to the first Ru–O coordination shell, while the peak at 2.50 Å is associated with the second shell's Ru–Ru and/or Ru–Mn coordination. Quantitative FT-EXAFS fitting of 12Ru/MnO$_2$ yielded a coordination number of 5.8 with a Ru–O average bond length ($d_{\text{Ru–O}}$) of 1.97 Å in the first shell, a coordination number of 2.8 with a Ru–Ru average bond length ($d_{\text{Ru–Ru}}$) of 3.07 Å in the second shell, and a coordination number of 0.5 with a Ru–Mn average bond length ($d_{\text{Ru–Mn}}$) of 2.97 Å in the second shell (Supplementary Figs. 5 and 6 and Supplementary Table 2). Fitting 4Ru/MnO$_2$ and 6Ru/MnO$_2$ reveals that their structure parameters in the first shell are similar to those of 12Ru/MnO$_2$. For the second shell, however, the contribution from Ru–Mn coordination becomes dominant at low Ru mass loadings.

The Ru–Ru coordination is absent for 4Ru/MnO_2, implying the notable presence of separated Ru atoms. This agrees with the HAADF-STEM results (Supplementary Fig. 7), which show many separated Ru atoms randomly distributed in 4Ru/MnO_2. The EXAFS fitting results demonstrate that the formation of Ru atom chains and arrays requires high Ru mass loading. To understand the origin of forming the Ru atom array, we have calculated the energetics of the Ru/MnO_2 model with different Ru dopings. Theoretical studies indicate that the formation of an ordered Ru structure is energetically more favourable than having the Ru atoms separated from each other in the MnO_2 when the Ru mass loading is high, that is, 13.6 wt% for the $Ru_8Mn_{56}O_{128}$ slab model. By contrast, the separated Ru configuration is more favourable at a low Ru mass loading condition, that is, 3.6 wt% for the $Ru_2Mn_{62}O_{128}$ slab model (Supplementary Fig. 8 and Supplementary Note 2), which agrees with the experimental observations.

X-ray absorption near-edge spectroscopy (XANES) spectra at the Ru K edge examined the chemical states of the Ru species (Supplementary Fig. 9a). The half-peak K-edge energy is used to estimate the valence. The Ru valence decreases from 3.56 to 3.36 as the Ru mass loading increases from 3.8 (4Ru/MnO_2) to 11.6 wt% (12Ru/MnO_2; Supplementary Fig. 9b). X-ray photoelectron spectroscopy (XPS) measurements were performed to further examine the valence state of the surface metal species (Supplementary Figs. 10 and 11). The Ru $3d_{5/2}$ peak of the commercial RuO_2 is centred at 281.5 eV, which matches the reported binding energy of Ru^{4+} species[32,33]. By comparison, the Ru $3d_{5/2}$ peaks of 4, 6 and 12Ru/MnO_2 slightly shift towards lower binding energies as Ru mass loading increases (Supplementary Table 3), suggesting that the Ru valence is close to four. Such a trend agrees with XANES analysis results. The Ru valence change can be attributed to the electronic interactions between Ru and MnO_2 (Supplementary Notes 3 and 4)[34].

Electrocatalytic performance. The OER performance of the 4, 6 and 12Ru/MnO_2 catalysts was evaluated in 0.1 M $HClO_4$ electrolyte by linear sweep voltammetry (LSV), and pure α-MnO_2, the commercial RuO_2 and homemade RuO_2 (details in Methods, Supplementary Fig. 12 and Supplementary Note 5) were used as references. Figure 3a,b shows the LSV curves and corresponding Tafel slopes, respectively. The 12Ru/MnO_2 catalyst delivers a η_{10} of 161 mV and a Tafel slope of 29.4 mV per decade (dec), which outperforms the homemade RuO_2 ($\eta_{10} = 250$ mV, 51.3 mV dec^{-1}), 4Ru/MnO_2 ($\eta_{10} = 286$ mV, 76.5 mV dec^{-1}) and 6Ru/MnO_2 ($\eta_{10} = 234$ mV, 44.7 mV dec^{-1}). The α-MnO_2 support shows nearly zero OER activity. Notably, the specific mass activity of the 12Ru/MnO_2 catalyst was calculated to be as high as 1,264.0 A g_{Ru}^{-1} at $\eta = 165$ mV, which is more than 600 times higher than that of RuO_2 (2.1 A g_{Ru}^{-1} at 165 mV; Supplementary Fig. 13). To further evaluate the intrinsic activity of the Ru species, the turnover frequency (TOF) was calculated (details in Methods) and plotted against the overpotential (Fig. 3c). The calculated TOF value of 1,192.3 h^{-1} for 12Ru/MnO_2 at $\eta = 165$ mV is at least one magnitude higher than those of 4Ru/MnO_2 (30.7 h^{-1}), 6Ru/MnO_2 (32.3 h^{-1}) and RuO_2 (2.0 h^{-1}). The OER activity normalized to the electrochemical surface area of the catalysts was also calculated (Supplementary Fig. 14). The specific activity of 12Ru/MnO_2 outperformed those of all the other samples. These results demonstrate the superior intrinsic OER catalytic activity of 12Ru/MnO_2.

The durability of the Ru/MnO_2 catalyst in acidic media is another key parameter for practical application. Figure 3d shows the chronopotentiometric response of the 12Ru/MnO_2 catalyst under a constant OER current density of 10 mA cm^{-2} recorded in an H-type water electrolysis cell with the anode and cathode separated by a Nafion 117 membrane. The η_{10} of 12Ru/MnO_2 was observed to increase monotonously from 161 to 330 mV throughout the continuous operation of 200 h. By contrast, rapid decay was observed in the activity of the homemade RuO_2 (inset in Fig. 3d). The metal ion concentration in the electrolyte was monitored using ICP-OES. The mass loss values of Ru and Mn in the 12Ru/MnO_2 catalyst after stable operation over long periods were as low as 0.50% and 0.28%, respectively. The Ru leaching loss is much lower than that of the recently reported Ru-based electrocatalysts (Supplementary Table 4)[7,14,35,36], validating its outstanding stability. We compared the performance of 12Ru/MnO_2 with previously reported OER electrocatalysts in terms of activity, noble metal loading and long-term stability. The 12Ru/MnO_2 performed better than the other listed OER electrocatalysts as shown in Fig. 3e and Supplementary Table 5. The catalyst stability was also tested under a constant large potential of 1.8 V. For the samples of homemade RuO_2, the commercial RuO_2 and IrO_2, a fast decay feature was normally observed along with the current retention of less than 11.3% for the initial 10 h; however, the 12Ru/MnO_2 exhibited a current retention of 75.3% for 40 h operation (Supplementary Fig. 15).

Analysis of OER process. The changes that occurred in the metal concentration in the electrolyte and the electrocatalyst structure were tracked to further understand the OER process. The electrolyte was collected from the anode and cathode sides of an H-type cell and analysed by ICP-OES (Supplementary Fig. 16 and Supplementary Note 6). Figure 4a shows the time dependence of the Ru and Mn molar concentrations when the electrolysis current density was set at 10 mA cm^{-2}. Nearly no Ru or Mn was detected on the cathode side. By contrast, the Ru concentration at the anode side underwent two periods of fluctuation during the first 4 h of electrolysis and then stabilized at a low level of approximately 0.04 μmol l^{-1}. The Mn concentration increased in the first 1.5 h and then remained at approximately 0.78 μmol l^{-1}. The initial fluctuations in the Ru concentration suggest that reconstruction of the electrocatalyst occurred. The spent 12Ru/MnO_2 catalyst was further characterized using STEM. Figure 4b and Supplementary Fig. 17 show annular bright-field STEM and the corresponding HAADF-STEM images, both of which indicate that the nanofibre morphology remained unchanged. Notably, distinctive patches of Ru atom arrays were observed on the surface of MnO_2 nanofibres (Supplementary Fig. 17). The locally intensified signal in the EDS mapping confirmed the presence of Ru atom arrays (Fig. 4c). Compared with fresh 12Ru/MnO_2, there is a minimal chance of observing Ru atom chains and irregular Ru nanoclusters in the spent electrocatalyst. The above results provide solid evidence for electrocatalyst reconstruction (Fig. 4e), which was driven by the cation exchange reaction that also occurred during the preparation of the electrocatalyst (Supplementary Fig. 2). The RuO_x nanoclusters were dissolved in the electrolyte, and the dissolved Ru ions were redeposited back into the MnO_2 at the cost of the partial leaching of Mn. However, unlike the catalyst preparation process, cation exchange occurred at a much lower Ru concentration under the reaction conditions, allowing the assembly of Ru atoms in the observed array. The formation of the Ru array is highly favourable for the OPM-type OER, which requires the presence of symmetrical metal sites for O–O coupling.

The dynamic cation exchange reaction between the Ru ions and the MnO_2 enhances the durability of 12Ru/MnO_2 because the leached Ru ions can be recaptured to support further reactions. However, such a reaction is unable to thoroughly describe the long-term attenuated activity (Fig. 3d) due to the thermodynamic instability of metal oxides[37]. To further understand the impact of reconstruction for the catalyst stability, XPS characterized that the peak position of Ru $3d_{5/2}$ shifted to higher binding energies in the spent 12Ru/MnO_2 (Supplementary Fig. 18a) in comparison to the fresh sample. The increase in the oxidation state of Ru after OER agrees with a previous report[38]. Notably, the Mn valence derived from the spectral splitting of the Mn 3*s* spectrum decreased from

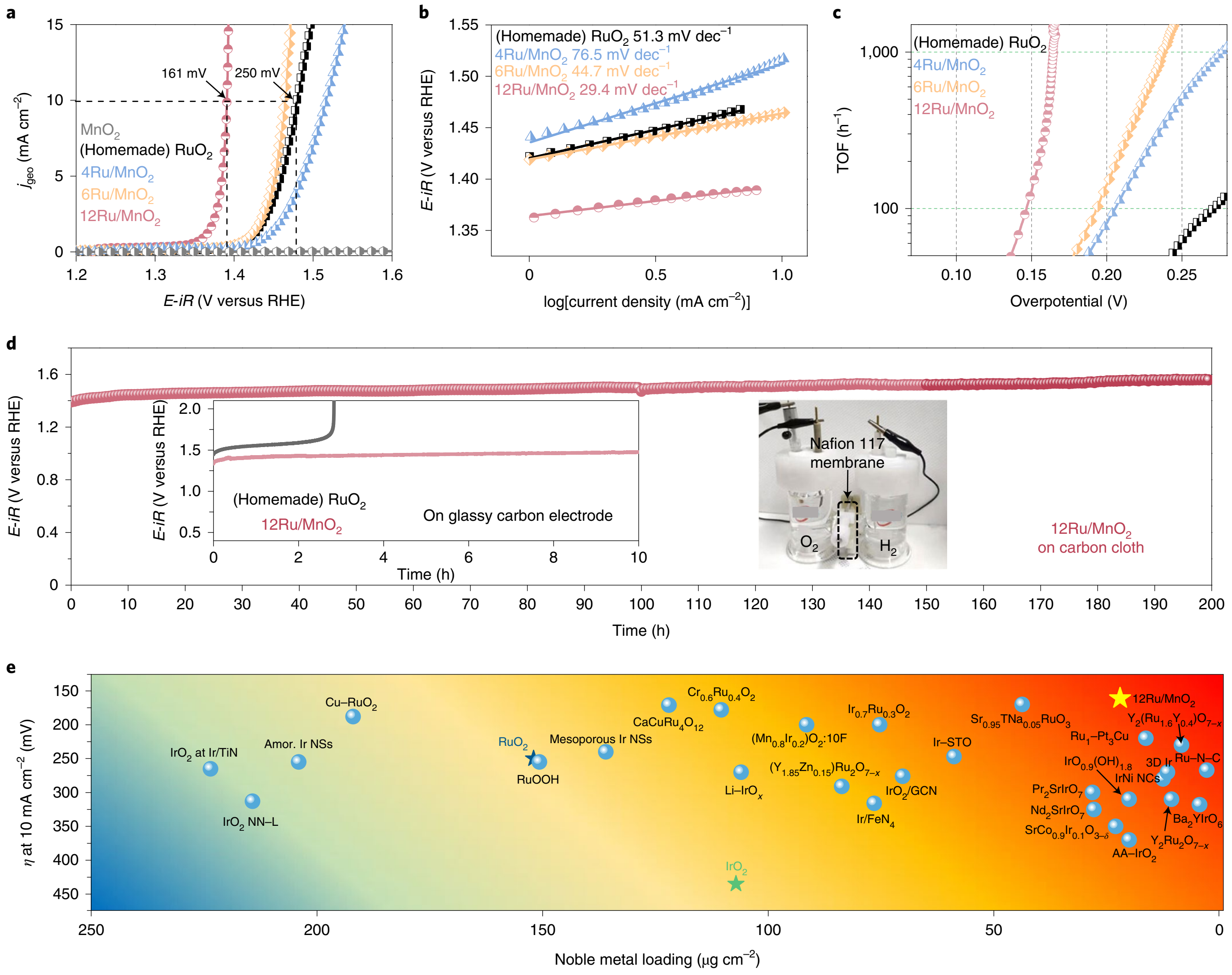

Fig. 3 | OER performance. **a**, Electrocatalytic OER performance of MnO$_2$, Ru/MnO$_2$ and homemade RuO$_2$ in 0.1 M HClO$_4$. **b**,**c**, Tafel slopes (**b**) and TOF (**c**) calculated from **a**. **d**, Chronopotentiometric response of the 12Ru/MnO$_2$ catalyst in an H-type cell (inset photo) using carbon cloth as a current collector. The chronopotentiometric response of 12Ru/MnO$_2$ and RuO$_2$ using gassy carbon as the current collector is shown in the inset. All the potential values were referenced using the RHE with ohmic drop correction. **e**, Comparison of OER activity for various reported electrocatalysts (Supplementary Table 5). The *x* and *y* axes represent the noble metal mass loading (including Pt, Ir and Ru) for electrocatalysts and the required overpotential at 10 mA cm^{-2}, respectively. Amor., amorphous; NN-L, long nano-needles; IrNSs, Ir nanosheets; GCN, graphitic carbon nitride; STO-Ir, iridium-containing strontium titanates; AA-IrO$_x$, quasi-amorphous ultra-pure Ir oxohydroxide (Alfa Aesar); 3D-Ir, three-dimensional Ir superstructure.

+3.89 for fresh 12Ru/MnO$_2$ to +3.69 for spent 12Ru/MnO$_2$, implying that the electronic metal–support interaction weakened after OER (Supplementary Fig. 18b). The decreased electron transfer from Mn to Ru can affect the OER performance in the spent 12Ru/MnO$_2$ (ref. [39]). In addition, the MnO$_2$ nanofibre support of a large surface area contains various defects such as step edges and kinks, which likely corrode more than the terrace sites as suggested by theoretical studies[40].

In the fresh sample of 12Ru/MnO$_2$, the Ru atoms tend to substitute for the undercoordinated Mn sites located at the defect sites such as step edges, which possess higher activity but are more prone to corrosion during the cation exchange process. The in-situ surface reconstruction during OER leads to dissolution and redeposition of Ru atoms back into more stable sites (for example, terrace site) but having lower activity. Time-dependent ICP-OES results coincide with the above hypothesis. The most pronounced reconstruction happened in the first 4 h, during which the increase rate in overpotential was the largest within the OER range of 200 h. We could also trace such a feature of surface reconstruction from the HAADF-STEM images. Many Ru chains and arrays are typically found to locate at the defective side edges of the fresh 12Ru/MnO$_2$ (Supplementary Fig. 4). By contrast, most Ru atoms were observed to locate not at the side edges but were likely move onto the energetically more stable sites of the nanofibre support in the spent electrocatalyst (Supplementary Fig. 17). Therefore, we conjecture that the observed stability attenuation of the Ru/MnO$_2$ stems from the combined effect of morphological (for example, surface defects) and electronic features.

Since the recorded current and the η_{10} calculation might be affected by the Ru reconstruction, we have estimated the corrosion current density by Ru oxidation and dissolution. A very small value of 14 µA cm^{-2} resulted using the ICP-OES data, but it would be reasonable to neglect it for the evaluation of OER performance (Methods for more details). The Faradaic efficiency (FE) of OER

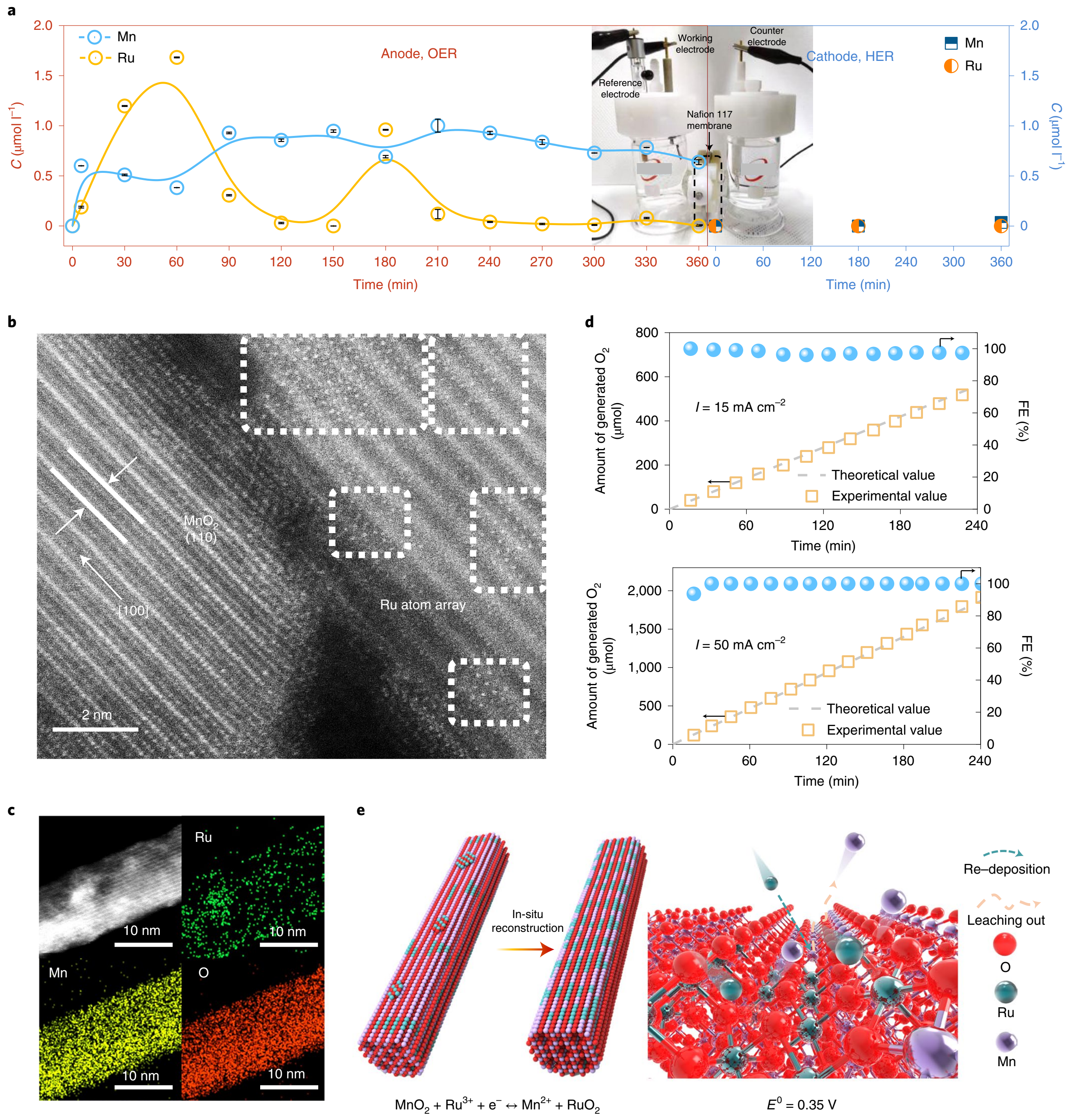

$MnO_2 + Ru^{3+} + e^- \leftrightarrow Mn^{2+} + RuO_2$ $E^0 = 0.35$ V

Fig. 4 | OER process analysis. a, Dependence of the Ru and Mn molar concentration in the electrolyte at the working electrode side (anode) and counter electrode side (cathode) on the OER reaction time. The OER current density was set at 10 mA cm^{-2}. A photograph of a homemade H-type cell is shown in the inset, in which the anode and cathode sides are separated by a Nafion 117 membrane. The error bars correspond to the standard deviation of three times of ICP-OES measurements. **b**, Aberration-corrected HAADF-STEM image of the spent 12Ru/MnO_2 catalyst. The white dashed boxes highlight the presence of Ru atom arrays. **c**, STEM image of the spent 12Ru/MnO_2 catalyst and the corresponding EDS element mapping images. **d**, The FE of 12Ru/MnO_2 as a function of reaction time determined by the water displacement method at current densities (j) of 15 and 50 mA cm^{-2}. **e**, Schematic illustration for the in-situ reconstruction process of Ru/MnO_2. E^0 represents the standard redox potentials at 298.15 K and a pressure of 1 atm.

was measured by rotating ring disc electrode (RRDE). The 12Ru/MnO_2 reached a FE of ~100% at 1.45 V, verifying our estimation. The efficiency decrease at higher potential stems from the accelerated generation of oxygen bubbles that reduce the detection efficiency at the ring (Supplementary Fig. 19). A long-term FE measurement of 12Ru/MnO_2 was also conducted for 4 h by collecting the generated oxygen. The measured oxygen volume fits well with the values calculated from Faraday's law of electrolysis, approaching ~97% and ~100% FE at current densities of 15 and 50 mA cm^{-2}, respectively (Fig. 4d).

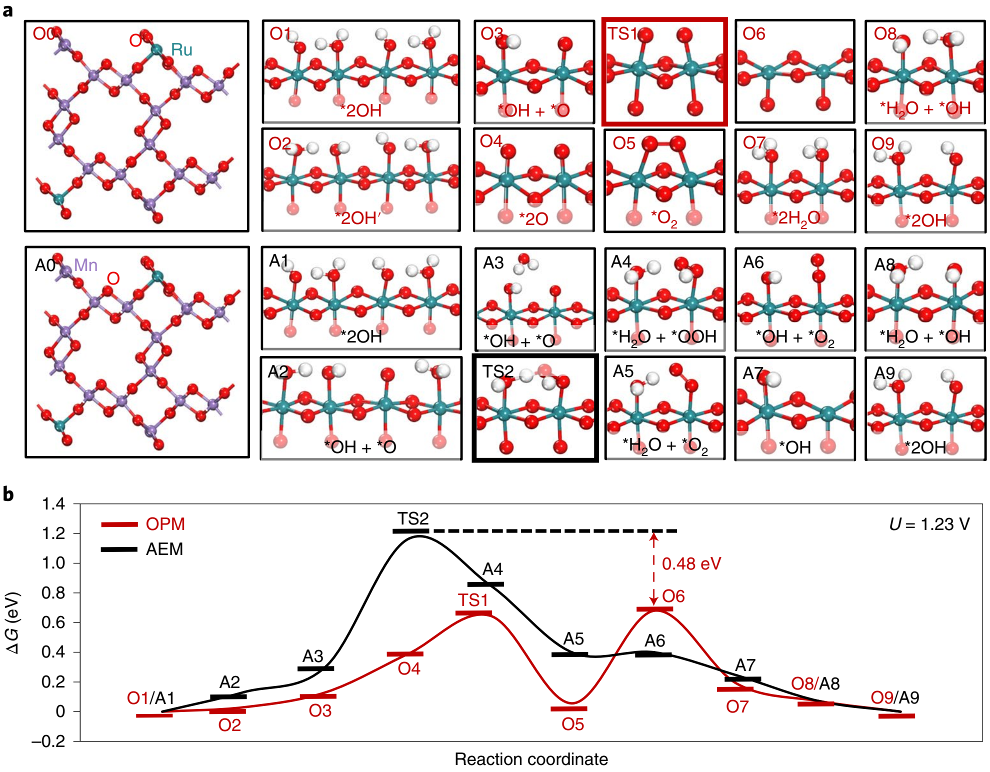

Fig. 5 | OER mechanism analysis based on DFT simulation results. a, Structures for key intermediates of OPM and AEM reaction pathways. **b**, The free energy (ΔG) diagrams of AEM and OPM at 1.23 V versus RHE. States O1–O9 and A1–A9 present the different elementary states in the OPM and AEM pathways, respectively. States O1 (*2OH) and O2 (*2OH′) differ in the positions of two OH groups. States O9/A9 are the same as the states O1/A1. TS stands for the transition state. Colours in the figure: green balls are Ru; violet balls are Mn; red balls are O; white balls are H.

Insights into OER mechanism. First-principles calculations were carried out to provide insight into the OER mechanism of Ru/MnO_2. In our experiments, the Ru mass loading for the 12Ru/MnO_2 sample was 11.6 wt%, and the HAADF-STEM observed a substantial proportion of α-MnO_2 (110) faces on the surface. According to these results, a Ru-doped MnO_2 (110) slab model with a formula of $Ru_8Mn_{56}O_{128}$ was constructed, corresponding to a 13.6 wt% Ru mass loading. To generate a reliable Ru-doped MnO_2 (110) surface structure, we first constructed six bulk unit cells for Ru-doped α-MnO_2 where the positions of Ru atoms were randomly selected. Then, we carried out a variable-cell relaxation for these unit cells. Our results show that the lattice parameters vary within 0.5% among various Ru configurations, while the density functional theory (DFT) energy varies within 0.4 eV. With the most stable unit cell, we cleaved the (110) slab model and then fixed the lattice parameters during subsequent surface-structure search and mechanistic studies. To evaluate the geometry accuracy of the DFT calculations, we performed a benchmark for RuO_2 and α-MnO_2. The error range of lattice parameters for the DFT calculations was only 2% for α-MnO_2 and 1% for RuO_2, so the Ru–Ru distance by the DFT calculations is reliable.

Using stochastic surface walking (SSW) global optimization and the neural network (NN) potential energy surface[41,42], we searched for the surface structure by exploring 10^4 minima (configuration energy spectrum in Supplementary Fig. 20 and Supplementary Table 6). The most stable surface structure is shown as O0 and A0 (Fig. 5a), with Ru atoms occupying the five-coordinated cationic sites on the surface with top coordinates with different oxygen-containing absorbates. Figure 5a illustrates the OER mechanism on the Ru sites of Ru-doped MnO_2, which follows the OPM and consists of nine elementary steps. The free energy changes for each elemental step are given in Supplementary Tables 7 and 8. First, a proton transfers from $^*H_2O$ to an adjacent $^*OH$, leading to two neighbouring $^*OH$ groups (O1 → O2). This step is slightly endothermic with a Gibbs free energy change of 0.03 eV. Next, two subsequent proton-coupled electron transfer steps occur in which the protons of two neighbouring $^*OH$ are released into the solution, leaving two $^*O$ (O2 → O3 → O4). The two $^*O$ bond together to form $^*O_2$, with a kinetic barrier of 0.26 eV (O4 → TS1 → O5, where TS means a transition state). This step is exothermic, producing 0.59 eV. Subsequently, the $^*O_2$ is desorbed from the surface, with a free energy change of 0.62 eV (O5 → O6), and two H_2O molecules are adsorbed onto the bare Ru sites, followed by two proton-coupled electron transfer steps in which two $^*OH$ groups are generated (O6 → O7 → O8 → O9). Finally, the initial state O1 is recovered. Overall, the O_2 desorption in the OPM is the rate-determining step, and two electron-transfer steps occur before the rate-determining step. As a result, this mechanism has a Tafel slope of 30.0 mV dec^{-1} (details in Methods), which is in excellent agreement with the experimental value of 29.4 mV dec^{-1} (Fig. 3b).

The energetic profiles of the AEM were also calculated, as shown in Fig. 5c. Our results show that the barrier of AEM is 1.16 eV (Supplementary Table 9), which is 0.48 eV higher than that of the OPM (TS2 in Fig. 5c). This result demonstrates that the OPM is more favourable than the AEM on Ru/MnO_2 during the OER process. We also evaluated the OER activity of Mn sites (Supplementary Fig. 21, Supplementary Note 7 and Supplementary Tables 10 and 11). The overall barrier of OER on Mn sites was 1.69 eV, which is 1.01 eV higher than the OPM pathway and 0.53 eV higher than the AEM pathway on the Ru sites. Experimentally, the inferior activity of the control sample 4Ru/MnO_2 consisting of separated Ru atoms also could exclude the synergy between Ru and neighbouring Mn

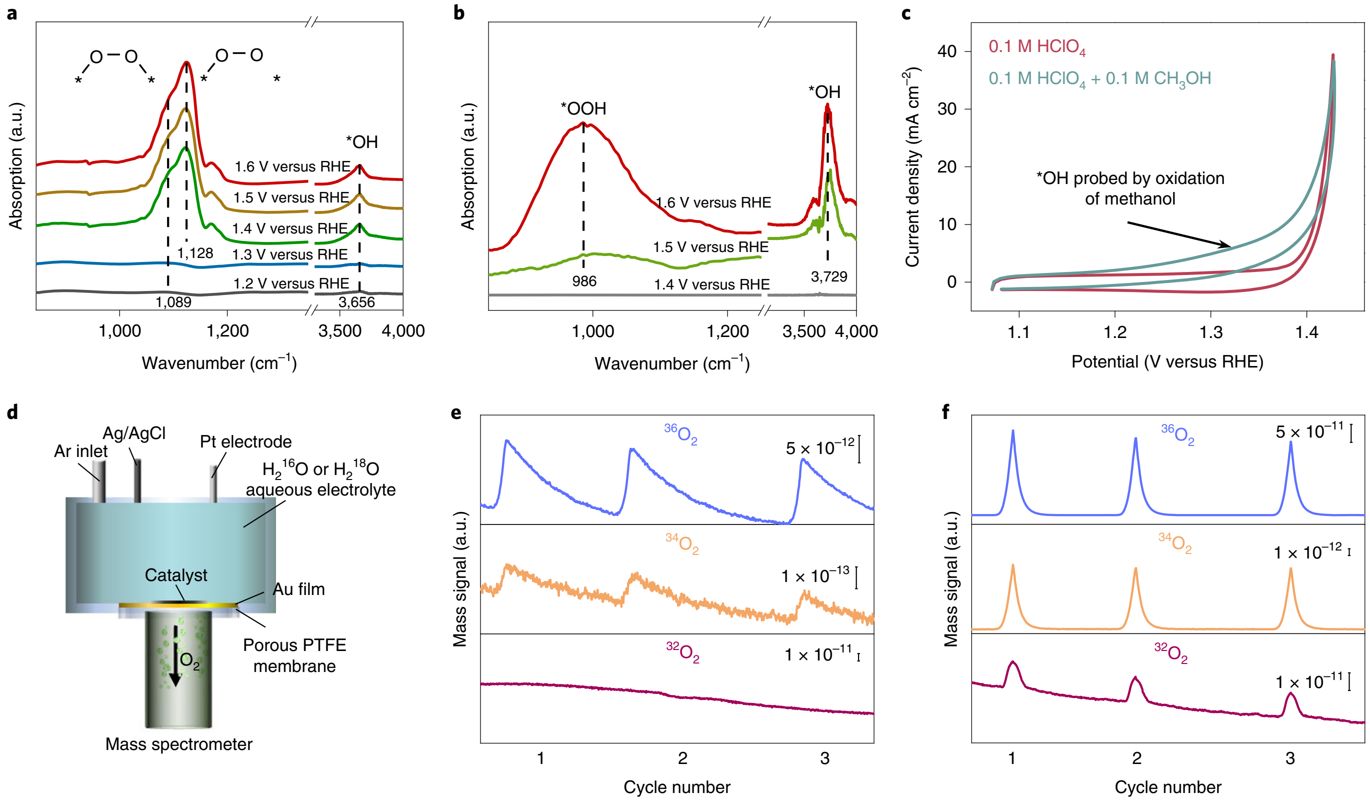

Fig. 6 | OER mechanism analysis. a,b, Operando synchrotron FTIR spectra recorded in the potential range of 1.2–1.6 V versus RHE for 12Ru/MnO_2 (**a**) and commercial RuO_2 (**b**). The * symbol represents catalytic sites. **c**, CV curves of 12Ru/MnO_2 recorded with and without 0.1 M methanol at a scan rate of 50 mV s^{-1}. **d**, Schematic illustration of the operando DEMS. PTFE, polytetrafluoroethylene. **e**,**f**, DEMS signals of O_2 products for 4Ru/MnO_2 (**e**) and 12Ru/MnO_2 (**f**) in the electrolyte using $H_2{}^{18}O$ as the solvent during three times of LSV in the potential range of 1.17–1.72 V versus RHE, with a 10 mV s^{-1} scan rate.

sites. Therefore, it is reasonable that the contribution of Mn sites to the total OER activity would be negligible.

A thermodynamic descriptor, that is, thermodynamic overpotential, is also widely adopted to estimate the activity of electrocatalysts in the literature[43,44]. The thermodynamic overpotential is determined by the most unfavourable Gibbs free energy change from all electroactive steps at the reversible potential. The theoretical overpotentials for the OPM and AEM pathways are 0.26 V (O3 → O4) and 0.31 V (A1 → A3), respectively, in our case validating that the OPM pathway is more favourable than the AEM pathway. Note that we do not rely on the thermodynamic overpotential to describe the OER activity in this work because it roughly estimates the activities while neglecting the kinetic barrier and a few non-electroactive steps.

To validate these theoretical results, we performed the operando EXAFS measurements of 12Ru/MnO_2 by switching the catalyst operation from open circuit potential to OER potentials (1.67–1.87 V versus a reversible hydrogen electrode (RHE)). Supplementary Fig. 22 shows that the peak positions of the first shell's Ru–O and the second shell's Ru–Ru revealed negligible variations, which is within the error range of the EXAFS technique. The bond lengths of the first shell's Ru–O and the second shell's Ru–Ru derived from the simulated structure models also showed a tiny variation for each OER elementary step (Supplementary Table 12), matching with the operando EXAFS results. By contrast, previous operando EXAFS work reported by Chen's group demonstrated that the bond length of the first shell's Ru–O decreased for RuO_2 during OER[45]. As a result, it would be reasonable that the operando EXAFS spectra not only suggest that the Ru atomic array remained structurally stable during OER, but also imply that 12Ru/MnO_2 follows a different OER pathway, in contrast to RuO_2.

To experimentally probe the OER mechanism, operando synchrotron FT infrared (FTIR) spectroscopy was carried out because it is susceptible to the change of surface reaction intermediates. The catalysts were uniformly dispersed on carbon paper and assembled in a homemade top-plate reflection infrared set-up developed by Liu's group (Supplementary Fig. 23)[46,47]. Figure 6a,b shows the operando synchrotron FTIR spectrum of 12Ru/MnO_2. A distinctive absorption peak at 1,128 cm^{-1} and a shoulder peak at 1,089 cm^{-1} were observed. The peak intensity dramatically increased as the potential reached the OER region (≥1.4 V), suggesting the generation of a large number of reaction intermediates. The shoulder peak (1,089 cm^{-1}) is ascribed to the formation of an O–O bond, which usually suggests forming oxygen bridges between metal sites in the OPM-type OER as reported in recent literature (Supplementary Table 13)[48,49]. The central peak at 1,128 cm^{-1} is assigned to linearly bonded superoxol species (metal–O–O)[50], which are the intermediate before releasing O_2. This feature agrees with the calculated OPM pathway, in which oxygen release is the rate-limiting step (O5 → O6). As a control, synchrotron FTIR measurements of the commercial RuO_2 were conducted (Fig. 6b). Typical Ru–OOH intermediates involved in the AEM-type OER were detected, so a distinctive peak was not observed at ~1,128 cm^{-1}. The *OH is a typical intermediate during OPM-type OER, and its potential-dependent characteristic peak can also be found at 3,656 cm^{-1} (Fig. 6a)[47]. As reported by Tao et al., the generated *OH intermediates are electrophiles, which can be detected by reacting with nucleophiles such as methanol (Supplementary Fig. 24)[51]. Figure 6c shows the recorded cyclic voltammetry (CV) cycles of 12Ru/MnO_2 before and after the methanol addition. The current density difference caused by the methanol suggests that the generated intermediate of *OH is consumed by methanol oxidation.

To further confirm the OPM, operando differential electrochemical mass spectrometry (DEMS) with isotope labelling measurements was carried out (Fig. 6d). We have designed two steps of DEMS experiments using $H_2{}^{18}O$ and $H_2{}^{16}O$ as the supporting solution (0.1 M $HClO_4$). At the first step, 4Ru/MnO_2 and 12Ru/MnO_2 were loaded on porous gas-permeable Au working electrodes and subjected to three LSV cycles (1.17–1.72 V versus RHE) in the $H_2{}^{18}O$ electrolyte (Supplementary Fig. 25). XPS studies show that both catalysts have a rich amount of surface oxygen adsorbates (O_{ads}; Supplementary Fig. 26). For the OPM-type OER, the $^{16}O_{ads}$ on neighbouring Ru sites show the probability of coupling together to form $^{32}O_2$ (Supplementary Fig. 27). Figure 6e,f shows the recorded mass signal of the OER gaseous products. The 12Ru/MnO_2 steadily produced $^{32}O_2$, $^{34}O_2$ and $^{36}O_2$ at each LSV cycle. The 4Ru/MnO_2 with isolated Ru atoms (Supplementary Fig. 7) produced $^{34}O_2$ and $^{36}O_2$. Note that the $^{32}O_2$ product signal was not distinguishable from the noise background as the OER proceeds through the non-OPM pathway (Fig. 6f and Supplementary Fig. 28). Then, the catalysts underwent five consecutive CV cycles for labelling ^{18}O on their surfaces.

At the second step, the catalysts were washed with abundant water and then operated in the $H_2{}^{16}O$ electrolyte. Once again, if the OPM worked for 12Ru/MnO_2, the remaining surface adsorbates (containing ^{18}O) would probably couple together to form the $^{36}O_2$ product, without any detection of $^{36}O_2$ product for 4Ru/MnO_2 (Supplementary Figs. 29 and 30). Indeed, the DEMS results were observed to agree with our prediction, as shown in Supplementary Fig. 31. Considering that both catalysts share a similar surface area (Supplementary Fig. 32), the influence of physically adsorbed $H_2{}^{18}O$ can be excluded during OER. In summary, the operando FTIR and DEMS successfully detected the reaction intermediates and the isotope-labelled products from the OPM-type OER in 12Ru/MnO_2. We propose that the OER in 12Ru/MnO_2 typically follows the OPM pathway based on the operando measurements and methanol oxidation probe reaction results.

The catalysts after chronopotentiometric measurements were also analysed by XPS. The major difference between the OPM and the AEM is the involvement of *OOH. Metal oxide electrocatalysts that proceed via AEM usually generate metal oxyhydroxide[52–54]. The O 1*s* spectrum describing fresh RuO_2 catalyst shows three main peaks that are centred at 529.7 eV, 531.1 eV and 533.1 eV, which can be attributed to lattice oxygen, surface oxygen species adsorbed onto the vacancies (O_{ads}) and adsorbed H_2O, respectively (Supplementary Fig. 33)[54–57]. The O 1*s* spectrum describing the spent RuO_2 has an obvious new peak at 532.6 eV, indicating the formation of Ru oxyhydroxide during the OER[58]. By contrast, the oxyhydroxide-related peak is not observed in the spectrum of spent 12Ru/MnO_2 catalyst. In short, the operando measurements together with the ex-situ characterization prove that the OER proceeds via the OPM mechanism in 12Ru/MnO_2.

Conclusions

In summary, we demonstrate that patches of Ru atom arrays supported by crystalline α-MnO_2 nanofibres, which were prepared using a one-step cation exchange strategy followed by in-situ self-reconstruction of the electrocatalyst, are highly active and acid-stable OER electrocatalysts. The intrinsic OER activity of Ru is more than 600 times higher than that of RuO_2. Extensive operando and ex-situ characterizations together with theoretical calculations prove that the OER on Ru/MnO_2 proceeds via the OPM, in which the key step involves direct O–O radical coupling. Such a unique reaction pathway allows the Ru/MnO_2 to overcome the overpotential limitations imposed by the conventional AEM mechanism. The dynamic cation exchange reaction between Ru ions and MnO_2 during OER not only triggers the self-reconstruction of the electrocatalyst, but also ensures that the leached Ru ions can be recaptured to support further reactions, resulting in enhanced corrosion resistance. Our results illustrate a route that can boost OER performance via engineering the geometric structure of the metal active sites.

Methods

Preparation of α-MnO_2 nanofibres. In a typical procedure for synthesizing α-MnO_2 nanofibres, 0.02 mol of $MnSO_4 \cdot 5H_2O$ (analytical reagent, AR), 0.02 mol of $(NH_4)_2S_2O_8$ (AR) and 0.06 mol of K_2SO_4 (AR) were dissolved in 70 ml H_2O. After vigorous stirring for 1 h, the mixture was transferred to an autoclave and heated at 140 °C for 12 h. After cooling to room temperature, the as-obtained dark brown powders were washed five times with deionized water, separated via vacuum filtration and dried overnight in an oven at 80 °C.

Preparation of the Ru/MnO_2 nanofibres. In a typical procedure, 1.15 mmol of MnO_2 nanofibres were dispersed in 20 ml H_2O and sonicated for 30 min. A certain amount of $RuCl_3 \cdot xH_2O$ (AR) was dissolved in 20 ml of H_2O. The $RuCl_3$ solution was injected into the MnO_2 suspension at room temperature under vigorous stirring. The reaction was continued for 12 h. The products were then collected by vacuum filtration and washed several times with deionized water. After drying in an oven at 80 °C, the products obtained were further annealed at 200 °C for 1 h in air. $RuCl_3$ concentrations of 2.41, 4.82 and 19.28 mmol l^{-1} were used for 4Ru/MnO_2, 6Ru/MnO_2 and 12Ru/MnO_2, respectively, with accurate Ru percentages at 3.8, 5.8 and 11.6 (determined by ICP-OES analysis).

Preparation of the homemade RuO_2. In a typical procedure, 0.75 g $RuCl_3 \cdot xH_2O$ (AR) was dissolved in a 140 ml mixed solution containing H_2O and methanol solution (v/v = 1:1). Then 1 M KOH was injected into the $RuCl_3$ solution to control the pH at approximately 7. After stirring for 1 h, the precipitate was collected via centrifugation and washed five times in a water and ethanol (v/v = 1:1) solution. After drying overnight at 80 °C, the black powder obtained was annealed at 500 °C for 5 h in air.

Electrochemical measurements of the OER. The OER performance was evaluated using a standard three-electrode cell equipped with an electrochemistry workstation (IviumStat, Ivium Technologies) in an O_2-saturated 0.1 M $HClO_4$ electrolyte. A saturated calomel electrode (saturated KCl) and Pt net were employed as the reference and counter electrode, respectively. The electrocatalysts (5.0 mg) were dispersed in a mixture of 1 ml of deionized water and isopropanol with a volume ratio of 3:1, with 20 µl of Nafion solution as a binder. After ultrasonication for 1 h, 8 µl of homogeneous ink was dropped on a glassy carbon electrode (area, 0.19625 cm^2) and fully dried in air at room temperature. The mass loadings of the electrocatalysts onto two types of electrodes including glassy carbon and carbon cloth were controlled at approximately 0.2 and 2.0 mg cm^{-2}, respectively. For the OER experiment, LSV with a scanning rate of 5 mV s^{-1} was measured in the potential range of 1.2–1.75 V versus RHE. Calibration of the saturated calomel reference electrode was performed by measuring the RHE potential under an H_2 atmosphere using a Pt wire as the working electrode[59]. CVs were performed at a scanning rate of 1 mV s^{-1}, and the thermodynamic potential for the hydrogen electrode reaction was obtained as the average value of the two potentials when the current crossed zero, as suggested in previous reports[60,61]. In 0.1 M $HClO_4$, $E_{RHE} = E_{SCE} + 0.264$ V and $\eta = E_{RHE} - 1.23$ V (Supplementary Fig. 34), where E_{RHE} and E_{SCE} are the potentials of the RHE and saturated calomel electrode, respectively. The ohmic drop correction was determined by impedance analysis. All potentials were referenced using the RHE with *iR* compensation, where *i* is the measured current and *R* is the uncompensated resistance as determined by electrochemical impedance spectroscopy.

Calculation of the mass activity. The mass activity ($j_{\text{mass activity}}$) of the Ru/MnO_2 and RuO_2 catalysts was determined using equation (1):

$$j_{\text{mass activity}} = \frac{j_{\text{geo}} \times A_{\text{geo}}}{m_{\text{Ru}}} \quad (1)$$

where m_{Ru} is the calculated Ru mass loaded onto glassy carbon based on the results of ICP-OES analysis, A_{geo} is the geometric area and j_{geo} is the geometric current density.

Calculation of TOF. The TOF of the Ru/MnO_2 and RuO_2 catalysts was calculated using equation (2):

$$\begin{aligned} \text{TOF}\left(\text{O}_2\ \text{h}^{-1}\right) &= 3,600 \times \text{TOF}\left(\text{O}_2\ \text{s}^{-1}\right) \\ &= 3,600 \times \frac{\text{O}_2\ \text{turnovers per}\ A_{\text{geo}}}{\text{Active sites per}\ A_{\text{geo}}} \end{aligned} \quad (2)$$

The O_2 turnover per geometric area was obtained from the geometric current density for the LSV polarization curves according to equation (3):

$$\text{O}_2\text{ turnover per }A_{\text{geo}} = j_{\text{geo}} \times \frac{1\text{ C s}^{-1}}{1{,}000\text{ mA}} \times \frac{1\text{ mol}}{96{,}485.3\text{ C}} \times \frac{1}{4} \times \frac{6.023 \times 10^{23}}{1\text{ mol O}_2} \quad (3)$$

All Ru atoms were assumed to be active sites. Therefore, the number of active sites per geometric area equals the number of Ru atoms per geometric area, which can be calculated from the results of the ICP-OES analysis.

Calculation of the specific current density per electrochemically active surface area. The electrochemically active surface area (ECSA) for all electrocatalysts was estimated from the electrochemical double-layer capacitance (C_{dl}) of the catalytic surface according to equation (4):

$$\text{ECSA} = \frac{C_{\text{dl}}}{C_{\text{s}}} \quad (4)$$

where C_{dl} was measured from the scan-rate-dependent CVs in the non-Faradaic region of 1.1–1.2 V versus RHE in 0.1 M $HClO_4$ with the scan rate of 10, 20, 40, 60, 80 and 100 mV s^{-1}. The C_{s} is the specific capacitance of the catalysts per unit area under identical electrolyte conditions with a typically reported value range (0.015–0.110 mF cm^{-2}) in acidic solution. The general specific capacitance of 0.035 mF cm^{-2} was used to estimate ECSA in this work.

The roughness factor (R_{f}) was derived from the estimated ECSA according to equation (5):

$$R_{\text{f}} = \frac{\text{ECSA}}{A_{\text{geo}}} \quad (5)$$

where A_{geo} is the geometric area of the glassy carbon electrode, which equals 0.19625 cm^2.

The specific current density per ECSA (j_{s}) was calculated as shown in equation (6):

$$j_{\text{s}} = \frac{j_{\text{geo}}}{R_{\text{f}}} \quad (6)$$

where j_{geo} is the geometric current density.

Operando DEMS with isotope labelling. The operando DEMS system is similar to the system recently reported by the Strasser group[62]. The set-up consists of two interconnected vacuum chambers, including a mass spectrometer chamber with a high vacuum and a second chamber with a mild vacuum. The second chamber is directly connected with the electrochemical cell that operates at ambient pressure. The pressure difference allows the in-situ generated oxygen to be drawn downward into the vacuum chamber for mass spectrometer analysis rather than to be released upward into the air. The working electrode is a Au film sputtered on a porous polytetrafluoroethylene membrane. The hydrophobic polytetrafluoroethylene membrane permits gas flow while rejecting liquid. A cold trap cooled with dry ice needs to be installed between the electrochemical cell and the vacuum chamber to trap the water vapour for avoiding potential damages to the mass spectrometer. The catalyst ink was directly dropped into the Au film and then dried. The electrochemical cell is a typical three-electrode system, and its volume is around 3 ml. The small volume is suitable for the isotope experiments. For isotope labelling studies, 2 ml of 0.1 M $HClO_4$ was prepared using $H_2^{18}O$ as the solvent. The catalysts including Ru/MnO_2 and the reference RuO_2 were subjected to three LSV cycles in the potential range of 1.17–1.72 V versus RHE at a scan rate of 10 mV s^{-1}, while the mass signals of the gaseous products $^{32}O_2$, $^{34}O_2$ and $^{36}O_2$ were recorded. Then, five consecutive CV cycles (1.17–1.72 V versus RHE at 10 mV s^{-1}) were applied for labelling the catalyst surface with ^{18}O. The catalysts were washed with abundant water ($H_2^{16}O$) to remove $H_2^{18}O$ molecules physically attached to the catalyst layer, while the ^{18}O-containing species that chemically bonded on the surface remained. The catalysts with isotope-labelled surface then operated in a normal electrolyte 0.1 M $HClO_4$ with $H_2^{16}O$ as the solvent. Again, the gaseous products including $^{32}O_2$, $^{34}O_2$ and $^{36}O_2$ were monitored by the mass spectrometer. Before the electrochemical measurements, all the electrolytes were purged with high-purity Ar to remove the dissolved oxygen.

Operando synchrotron FTIR. The operando synchrotron radiation FTIR measurements were performed at beamline BL01B of the National Synchrotron Radiation Facility, Hefei, China. The homemade top-plate cell was reported by Liu's group[46,47]. The catalyst ink was dropped onto a carbon paper electrode and then dried. A thin layer of aqueous electrolyte was coated on the carbon paper working electrode to reduce the loss of infrared light. The FTIR data were recorded in a reflection mode to obtain high-quality spectra. The maximum spectral resolution is 2 cm^{-1}. Before data collection, a voltage was applied to the working electrode for around 20 min to test for receiving a reliable signal. The background spectrum of the working electrode was recorded at an open circuit condition. The recorded spectrum was processed by the OPUS software.

Theoretical calculation details. The fixed-cell SSW-NN method was used to explore the most stable structure of the α-MnO_2 surface. SSW global optimization aims to explore the potential energy surface (PES) and locate global/local minima, while the NN potential energy surface is trained based on the DFT dataset and delivers a high-speed PES evaluation, which provides a general solution for PES scanning with both high efficiency and high accuracy. The SSW-NN calculations were carried out using the Large-scale Atomic Simulation with neural network Potential[63,64]. All DFT calculations were carried out within the periodic plane-wave framework implemented by the Vienna Ab initio Simulation Package[65]. The electron–ion interaction was represented by the projector augmented wave, and the Hubbard-term-corrected DFT functional, PBE + U (refs. [66,67]), was utilized. The effective Hubbard term (U_{eff}) was set at 4.0 eV for Mn according to the linear response approach[68–70]. The details of SSW-NN and DFT calculations are given in the Supplementary Information. The Ru-doped MnO_2 slab consists of $Ru_8Mn_{56}O_{128}$ and has a rectangular surface cell with dimensions of 11.83 × 14.13 Å^2. The transition states were determined using the constrained Broyden dimer method[42,71,72]. Spin polarization with an antiferromagnetic configuration was utilized for α-MnO_2 systems. The solvation effect that is due to the long-range electrostatic interaction was modelled by a periodic continuum solvation model with a modified Poisson–Boltzmann equation[73–75]. The computational hydrogen electrode approach[43,76–79] was utilized to estimate the energetic profiles of the OER. All the reported free energy changes in the OER refer to the electrode potential (U) at 1.23 V versus RHE.

Calculation of the average oxidation state of Mn. The magnitude of the splitting energy of the Mn 3s peaks is approximately linear to the Mn oxidation state[80]:

$$\Delta E = 7.88 - 0.85n \quad (7)$$

where ΔE is the Mn 3s multiplet splitting energies and n is the average oxidation state of the Mn ($2 \leq n \leq 4$). Thus, the average oxidation state of Mn can be determined using equation (8):

$$n = \frac{7.88 - \Delta E}{0.85} \quad (8)$$

Estimation of the Tafel slopes. The Tafel slope is calculated by the Tafel equation (equations (9)–(11))[81,82]:

$$\eta = a + b \log i \quad (9)$$

$$b = \frac{\partial \eta}{\partial \log i} = \frac{2.303RT}{\alpha F} \quad (10)$$

$$\alpha = \frac{n_{\text{b}}}{\upsilon} + n_{\text{r}}\beta \quad (11)$$

where η is the overpotential; a is the Tafel constant; b is the Tafel slope; i is the current; T is the temperature in kelvin (K); R is the ideal gas constant; α is the transfer coefficient; F is the Faraday constant; n_{b} is the number of electrons transferred before the rate-determining step; υ is the number of rate-determining steps in the overall reaction; n_{r} is the number of electrons participating in the rate-determining step; and β is the symmetry factor, which is often around 0.5. With the reaction mechanism, we derive the parameters $n_{\text{b}} = 2$, $\upsilon = 1$ and $n_{\text{r}} = 0$, which imply a Tafel slope of 30.0 mV dec^{-1}.

Estimation of the Ru corrosion current. The chronopotentiometric measurement of 12Ru/MnO_2 (mass loading of 0.2 mg cm^{-2}) for 1 h at a constant current density of 10 mA cm^{-2} was conducted. Based on monitoring the Ru concentration in the electrolyte by ICP-OES, Ru dissolves at an average rate of 3.7 ng cm^{-2} s^{-1}. Moreover, we assume that the dissolved Ru in the form of the unknown Ru^{x+} species has the highest valency of +8, such as in the case of soluble H_2RuO_5, and that its primary oxidation reaction during OER is around four-electron in nature. Then, the corrosion current density of Ru can be estimated as

$$j = 3.7 \times 10^{-3}\ \mu\text{g}_{\text{Ru}}\ \text{cm}^{-2}\ \text{s}^{-1} \times \frac{4F}{M_{\text{Ru}}} \approx 14\ \mu\text{A cm}^{-2} \quad (12)$$

where $M_{\text{Ru}} = 101.07\ \text{g}_{\text{Ru}}\ \text{mol}^{-1}$ is the molar mass of Ru and $F = 96{,}485\ \text{C mol}^{-1}$ is the Faraday constant.

OER FE measured by RRDE. The RRDE experiments were carried out with the electrolyte saturated with nitrogen, which was purged for at least 30 min before the experiment and kept passing the electrolyte during the measurement. For RRDE measurements, the Pt-ring/glassy-carbon-disc electrode with a catalyst loading of 15 μg cm^{-2} was used as the working electrode[83]. The FE (%) was calculated according to previous reports[83,84]:

$$\text{FE}(\%) = \frac{\frac{4}{n_{\text{ORR}}} i_{\text{ring}}}{N\, i_{\text{disc}}} \times 100 \quad (13)$$

where $4/n_{\text{ORR}}$ is the ratio of the electron transferred numbers in the OER at the disk and in the ORR at the ring electrode. n_{ORR} equals 4 for a Pt ring. i_{disc} is the disc current, which was corrected by excluding the capacity contribution. i_{ring} is the ring current, which was corrected for the background currents. N is the ring collection efficiency (36%), which was obtained from experiments with the redox couple $(Fe(CN)_6)^{3-}$/ $(Fe(CN)_6)^{4-}$ and closely matches with the theoretical collection efficiency (37%).

FE determined by water displacement method. The FE was calculated by the equation as follows:

$$\mathrm{FE}(\%) = \frac{\text{Experimental of } O_2}{\text{Theoretical of } O_2} \times 100 \qquad (14)$$

The theoretical amount of O_2 gas (n_T) was calculated by Faraday's law:

$$n_T = \frac{I \times t}{z \times F} \qquad (15)$$

where n_T is in moles, I is the current (A), t is the OER reaction time (s), z is the electron transfer number of OER ($z=4$) and F is the Faraday constant.

The experimental amount of O_2 (n_E) gas was determined by a water displacement method and calculated by the ideal gas law:

$$n_E = \frac{P \times V}{R \times T} \qquad (16)$$

where n_E is in moles, V is the volume of gaseous product in liters (l), T is the temperature in kelvin (K), R is the ideal gas constant and the P is the partial pressure of O_2; the partial pressure in our calculations is determined by

$$P_{\text{Oxygen}} = \frac{P_{\text{Total}} - P_{\text{Water}}}{P_{\text{Total}}} \times 1\,\text{atm} \qquad (17)$$

where P_{Water} is 21.1 mm Hg and P_{Total} is 762 mm Hg (ref. [85]).

Data availability

Source data are provided with this paper. The data supporting the findings of this study are available within the article and its Supplementary Information or from the corresponding authors upon reasonable request.

Code availability

The software codes for Large-scale Atomic Simulation with neural network Potential and the NN potentials used within the article are available from the corresponding authors upon request or on the website http://www.lasphub.com.

Received: 22 March 2021; Accepted: 12 October 2021;
Published online: 17 December 2021

References

1. King, L. A. et al. A non-precious metal hydrogen catalyst in a commercial polymer electrolyte membrane electrolyser. *Nat. Nanotechnol.* **14**, 1071–1074 (2019).
2. Seitz, L. C. et al. A highly active and stable $IrO_x/SrIrO_3$ catalyst for the oxygen evolution reaction. *Science* **353**, 1011–1014 (2016).
3. Li, A. et al. Stable potential windows for long-term electrocatalysis by manganese oxides under acidic conditions. *Angew. Chem. Int. Ed.* **58**, 5054–5058 (2019).
4. *Johnson Matthey Price Charts* (Johnson Matthey, accessed 15 December 2020); www.platinum.matthey.com/prices/price-charts#
5. Rao, R. R. et al. Operando identification of site-dependent water oxidation activity on ruthenium dioxide single-crystal surfaces. *Nat. Catal.* **3**, 516–525 (2020).
6. Stoerzinger, K. A. et al. The role of Ru redox in pH-dependent oxygen evolution on rutile ruthenium dioxide surfaces. *Chem* **2**, 668–675 (2017).
7. Yao, Y. et al. Engineering the electronic structure of single atom Ru sites via compressive strain boosts acidic water oxidation electrocatalysis. *Nat. Catal.* **2**, 304–313 (2019).
8. Reier, T., Nong, H. N., Teschner, D., Schlögl, R. & Strasser, P. Electrocatalytic oxygen evolution reaction in acidic environments – reaction mechanisms and catalysts. *Adv. Energy Mater.* **7**, 1601275 (2017).
9. Song, J. et al. A review on fundamentals for designing oxygen evolution electrocatalysts. *Chem. Soc. Rev.* **49**, 2196–2214 (2020).
10. Koper, M. T. M. Theory of multiple proton–electron transfer reactions and its implications for electrocatalysis. *Chem. Sci.* **4**, 2710–2723 (2013).
11. Rossmeisl, J., Qu, Z. W., Zhu, H., Kroes, G. J. & Nørskov, J. K. Electrolysis of water on oxide surfaces. *J. Electroanal. Chem.* **607**, 83–89 (2007).
12. Huang, Z.-F. et al. Strategies to break the scaling relation toward enhanced oxygen electrocatalysis. *Matter* **1**, 1494–1518 (2019).
13. Hao, S. et al. Dopants fixation of ruthenium for boosting acidic oxygen evolution stability and activity. *Nat. Commun.* **11**, 5368 (2020).
14. Chen, H. et al. Optimization of active sites via crystal phase, composition, and morphology for efficient low-iridium oxygen evolution catalysts. *Angew. Chem. Int. Ed.* **59**, 19654–19658 (2020).
15. Shan, J. et al. Charge-redistribution-enhanced nanocrystalline Ru@IrO_x electrocatalysts for oxygen evolution in acidic media. *Chem* **5**, 445–459 (2019).
16. Shan, J., Ling, T., Davey, K., Zheng, Y. & Qiao, S.-Z. Transition-metal-doped RuIr bifunctional nanocrystals for overall water splitting in acidic environments. *Adv. Mater.* **31**, 1900510 (2019).
17. Zhang, B. et al. Homogeneously dispersed multimetal oxygen-evolving catalysts. *Science* **352**, 333–337 (2016).
18. Wang, J. et al. Amorphization activated ruthenium-tellurium nanorods for efficient water splitting. *Nat. Commun.* **10**, 5692 (2019).
19. Kim, M., Park, J., Kang, M., Kim, J. Y. & Lee, S. W. Toward efficient electrocatalytic oxygen evolution: emerging opportunities with metallic pyrochlore oxides for electrocatalysts and conductive supports. *ACS Cent. Sci.* **6**, 880–891 (2020).
20. Huang, Z.-F. et al. Chemical and structural origin of lattice oxygen oxidation in Co–Zn oxyhydroxide oxygen evolution electrocatalysts. *Nat. Energy* **4**, 329–338 (2019).
21. Bockris, J. O. M. Kinetics of activation controlled consecutive electrochemical reactions: anodic evolution of oxygen. *J. Chem. Phys.* **24**, 817–827 (1956).
22. Song, F. et al. An unconventional iron nickel catalyst for the oxygen evolution reaction. *ACS Cent. Sci.* **5**, 558–568 (2019).
23. Garrido-Barros, P., Gimbert-Suriñach, C., Matheu, R., Sala, X. & Llobet, A. How to make an efficient and robust molecular catalyst for water oxidation. *Chem. Soc. Rev.* **46**, 6088–6098 (2017).
24. Roy, C. et al. Trends in activity and dissolution on RuO_2 under oxygen evolution conditions: particles versus well-defined extended surfaces. *ACS Energy Lett.* **3**, 2045–2051 (2018).
25. Hodnik, N. et al. New insights into corrosion of ruthenium and ruthenium oxide nanoparticles in acidic media. *J. Phys. Chem. C* **119**, 10140–10147 (2015).
26. Rong, X., Parolin, J. & Kolpak, A. M. A fundamental relationship between reaction mechanism and stability in metal oxide catalysts for oxygen evolution. *ACS Catal.* **6**, 1153–1158 (2016).
27. Kodera, M. et al. Reversible O–O bond scission of peroxodiiron(III) to high-spin oxodiiron(IV) in dioxygen activation of a diiron center with a bis-tpa dinucleating ligand as a soluble methane monooxygenase model. *J. Am. Chem. Soc.* **134**, 13236–13239 (2012).
28. Okamura, M. et al. A pentanuclear iron catalyst designed for water oxidation. *Nature* **530**, 465–468 (2016).
29. Zhang, H. et al. Enhanced interactions between gold and MnO_2 nanowires for water oxidation: a comparison of different chemical and physical preparation methods. *ACS Sustain. Chem. Eng.* **3**, 2049–2057 (2015).
30. Ling, T., Jaroniec, M. & Qiao, S.-Z. Recent progress in engineering the atomic and electronic structure of electrocatalysts via cation exchange reactions. *Adv. Mater.* **32**, 2001866 (2020).
31. Lübke, M. et al. Transition-metal-doped α-MnO_2 nanorods as bifunctional catalysts for efficient oxygen reduction and evolution reactions. *ChemistrySelect* **3**, 2613–2622 (2018).
32. Morgan, D. J. Resolving ruthenium: XPS studies of common ruthenium materials. *Surf. Interface Anal.* **47**, 1072–1079 (2015).
33. Liu, X. et al. Electrochemo-mechanical effects on structural integrity of Ni-rich cathodes with different microstructures in all solid-state batteries. *Adv. Energy Mater.* **11**, 2003583 (2021).
34. Guo, Y. et al. Low-temperature CO_2 methanation over CeO_2-supported Ru single atoms, nanoclusters, and nanoparticles competitively tuned by strong metal–support interactions and H-spillover effect. *ACS Catal.* **8**, 6203–6215 (2018).
35. Miao, X. et al. Quadruple perovskite ruthenate as a highly efficient catalyst for acidic water oxidation. *Nat. Commun.* **10**, 3809 (2019).
36. Cao, L. et al. Dynamic oxygen adsorption on single-atomic ruthenium catalyst with high performance for acidic oxygen evolution reaction. *Nat. Commun.* **10**, 4849 (2019).
37. Binninger, T. et al. Thermodynamic explanation of the universal correlation between oxygen evolution activity and corrosion of oxide catalysts. *Sci. Rep.* **5**, 12167 (2015).
38. Kötz, R., Lewerenz, H. J. & Stucki, S. XPS studies of oxygen evolution on Ru and RuO_2 anodes. *J. Electrochem. Soc.* **130**, 825–829 (1983).
39. Kwon, T. et al. Interfacing RuO_2 with Pt to induce efficient charge transfer from Pt to RuO_2 for highly efficient and stable oxygen evolution in acidic media. *J. Mater. Chem. A* **9**, 14352–14362 (2021).
40. Frydendal, R., Paoli, E. A., Chorkendorff, I., Rossmeisl, J. & Stephens, I. E. L. Toward an active and stable catalyst for oxygen evolution in acidic media: Ti-stabilized MnO_2. *Adv. Energy Mater.* **5**, 1500991 (2015).
41. Huang, S.-D., Shang, C., Zhang, X.-J. & Liu, Z.-P. Material discovery by combining stochastic surface walking global optimization with a neural network. *Chem. Sci.* **8**, 6327–6337 (2017).
42. Shang, C., Zhang, X.-J. & Liu, Z.-P. Stochastic surface walking method for crystal structure and phase transition pathway prediction. *Phys. Chem. Chem. Phys.* **16**, 17845–17856 (2014).

43. García-Mota, M. et al. Tailoring the activity for oxygen evolution electrocatalysis on rutile TiO_2(110) by transition-metal substitution. *ChemCatChem* **3**, 1607–1611 (2011).
44. Friebel, D. et al. Identification of highly active Fe sites in (Ni,Fe)OOH for electrocatalytic water splitting. *J. Am. Chem. Soc.* **137**, 1305–1313 (2015).
45. Chang, C.-J., Chu, Y.-C., Yan, H.-Y., Liao, Y.-F. & Chen, H. M. Revealing the structural transformation of rutile RuO_2 *via in situ* X-ray absorption spectroscopy during the oxygen evolution reaction. *Dalton Trans.* **48**, 7122–7129 (2019).
46. Cheng, W. et al. Lattice-strained metal–organic-framework arrays for bifunctional oxygen electrocatalysis. *Nat. Energy* **4**, 115–122 (2019).
47. Su, H. et al. Dynamic evolution of solid–liquid electrochemical interfaces over single-atom active sites. *J. Am. Chem. Soc.* **142**, 12306–12313 (2020).
48. Lang, C. et al. Observation of a potential-dependent switch of water-oxidation mechanism on Co-oxide-based catalysts. *Chem* https://doi.org/10.1016/j.chempr.2021.03.015 (2021).
49. Wang, B. et al. *In situ* structural evolution of the multi-site alloy electrocatalyst to manipulate the intermediate for enhanced water oxidation reaction. *Energy Environ. Sci.* **13**, 2200–2208 (2020).
50. Vivek, J. P., Berry, N. G., Zou, J., Nichols, R. J. & Hardwick, L. J. In situ surface-enhanced infrared spectroscopy to identify oxygen reduction products in nonaqueous metal–oxygen batteries. *J. Phys. Chem. C* **121**, 19657–19667 (2017).
51. Tao, H. B. et al. A general method to probe oxygen evolution intermediates at operating conditions. *Joule* **3**, 1498–1509 (2019).
52. Zhang, N. et al. Lattice oxygen activation enabled by high-valence metal sites for enhanced water oxidation. *Nat. Commun.* **11**, 4066 (2020).
53. Pfeifer, V. et al. *In situ* observation of reactive oxygen species forming on oxygen-evolving iridium surfaces. *Chem. Sci.* **8**, 2143–2149 (2017).
54. Liang, C. et al. Exceptional performance of hierarchical Ni–Fe oxyhydroxide@NiFe alloy nanowire array electrocatalysts for large current density water splitting. *Energy Environ. Sci.* **13**, 86–95 (2020).
55. Kuznetsov, D. A. et al. Tailoring lattice oxygen binding in ruthenium pyrochlores to enhance oxygen evolution activity. *J. Am. Chem. Soc.* **142**, 7883–7888 (2020).
56. Wang, J. et al. Boosting the electrocatalytic activity of Co_3O_4 nanosheets for a Li-O_2 battery through modulating inner oxygen vacancy and exterior Co^{3+}/Co^{2+} ratio. *ACS Catal.* **7**, 6533–6541 (2017).
57. Bao, J. et al. Ultrathin spinel-structured nanosheets rich in oxygen deficiencies for enhanced electrocatalytic water oxidation. *Angew. Chem. Int. Ed.* **54**, 7399–7404 (2015).
58. Näslund, L.-Å., Ingason, Á. S., Holmin, S. & Rosen, J. Formation of $RuO(OH)_2$ on RuO_2-based electrodes for hydrogen production. *J. Phys. Chem. C* **118**, 15315–15323 (2014).
59. Liang, Y. et al. Co_3O_4 nanocrystals on graphene as a synergistic catalyst for oxygen reduction reaction. *Nat. Mater.* **10**, 780–786 (2011).
60. Lei, C. et al. Fe-N_4 sites embedded into carbon nanofiber integrated with electrochemically exfoliated graphene for oxygen evolution in acidic medium. *Adv. Energy Mater.* **8**, 1801912 (2018).
61. Xu, X., Song, F. & Hu, X. A nickel iron diselenide-derived efficient oxygen-evolution catalyst. *Nat. Commun.* **7**, 12324 (2016).
62. Görlin, M. et al. Oxygen evolution reaction dynamics, Faradaic charge efficiency, and the active metal redox states of Ni–Fe oxide water splitting electrocatalysts. *J. Am. Chem. Soc.* **138**, 5603–5614 (2016).
63. Huang, S.-D., Shang, C., Kang, P.-L. & Liu, Z.-P. Atomic structure of boron resolved using machine learning and global sampling. *Chem. Sci.* **9**, 8644–8655 (2018).
64. Huang, S.-D., Shang, C., Kang, P.-L., Zhang, X.-J. & Liu, Z.-P. LASP: fast global potential energy surface exploration. *WIREs Comput. Mol. Sci.* **9**, e1415 (2019).
65. Kresse, G. & Furthmüller, J. Efficient iterative schemes for *ab initio* total-energy calculations using a plane-wave basis set. *Phys. Rev. B* **54**, 11169–11186 (1996).
66. Perdew, J. P., Burke, K. & Ernzerhof, M. Generalized gradient approximation made simple. *Phys. Rev. Lett.* **77**, 3865–3868 (1996).
67. Anisimov, V. I., Zaanen, J. & Andersen, O. K. Band theory and Mott insulators: Hubbard U instead of Stoner I. *Phys. Rev. B* **44**, 943–954 (1991).
68. Cococcioni, M. & De Gironcoli, S. Linear response approach to the calculation of the effective interaction parameters in the LDA + U method. *Phys. Rev. B* **71**, 035105 (2005).
69. García-Mota, M. et al. Importance of correlation in determining electrocatalytic oxygen evolution activity on cobalt oxides. *J. Phys. Chem. C* **116**, 21077–21082 (2012).
70. Li, Y.-F. & Selloni, A. Mechanism and activity of water oxidation on selected surfaces of pure and Fe-doped NiO_x. *ACS Catal.* **4**, 1148–1153 (2014).
71. Shang, C. & Liu, Z. P. Stochastic surface walking method for structure prediction and pathway searching. *J. Chem. Theory Comput.* **9**, 1838–1845 (2013).
72. Shang, C. & Liu, Z.-P. Constrained Broyden minimization combined with the dimer method for locating transition state of complex reactions. *J. Chem. Theo. Comput.* **6**, 1136–1144 (2010).
73. Fattebert, J. L. & Gygi, F. Linear-scaling first-principles molecular dynamics with plane-waves accuracy. *Phys. Rev. B* **73**, 115124 (2006).
74. Fang, Y. H. & Liu, Z. P. Mechanism and Tafel lines of electro-oxidation of water to oxygen on RuO_2(110). *J. Am. Chem. Soc.* **132**, 18214–18222 (2010).
75. Walter, M. G. et al. Solar water splitting cells. *Chem. Rev.* **110**, 6446–6473 (2010).
76. Li, Y.-F. & Liu, Z.-P. Particle size, shape and activity for photocatalysis on titania anatase nanoparticles in aqueous surroundings. *J. Am. Chem. Soc.* **133**, 15743–15752 (2011).
77. You, B., Jiang, N., Sheng, M., Bhushan, M. W. & Sun, Y. Hierarchically porous urchin-like Ni_2P superstructures supported on nickel foam as efficient bifunctional electrocatalysts for overall water splitting. *ACS Catal.* **6**, 714–721 (2016).
78. Li, Y.-F. & Liu, Z.-P. Active site revealed for water oxidation on electrochemically induced δ-MnO_2: role of spinel-to-layer phase transition. *J. Am. Chem. Soc.* **140**, 1783–1792 (2018).
79. Li, Y.-F., Liu, Z.-P., Liu, L. & Gao, W. Mechanism and activity of photocatalytic oxygen evolution on titania anatase in aqueous surroundings. *J. Am. Chem. Soc.* **132**, 13008–13015 (2010).
80. Gao, T. et al. Synthesis and properties of layered-structured Mn_5O_8 nanorods. *J. Phys. Chem. C* **114**, 922–928 (2010).
81. Suen, N. T. et al. Electrocatalysis for the oxygen evolution reaction: recent development and future perspectives. *Chem. Soc. Rev.* **46**, 337–365 (2017).
82. Burstein, G. T. A century of Tafel's equation: a commemorative issue of corrosion science. *Corros. Sci.* **47**, 2855–2856 (2005).
83. & Forslund, R. P. et al. Exceptional electrocatalytic oxygen evolution via tunable charge transfer interactions in $La_{0.5}Sr_{1.5}Ni_{1-x}Fe_xO_{4\pm\delta}$ Ruddlesden–Popper oxides. *Nat. Commun.* **9**, 3150 (2018).
84. Naresh Kumar, T., Sivabalan, S., Chandrasekaran, N. & Phani, K. L. Synergism between polyurethane and polydopamine in the synthesis of Ni–Fe alloy monoliths. *Chem. Commun.* **51**, 1922–1925 (2015).
85. Sultan, S. et al. Superb water splitting activity of the electrocatalyst $Fe_3Co(PO_4)_4$ designed with computation aid. *Nat. Commun.* **10**, 5195 (2019).

Acknowledgements

J.-H.L. appreciates the support from the Creative Materials Discovery Program through the National Research Foundation of Korea funded by the Ministry of Science and ICT (2018M3D1A1057844). X.L. acknowledges financial support from the National Natural Science Foundation of China (no. 21972163), the Fundamental Research Funds for the Central Universities, the DHU Distinguished Young Professor Program, the Development Fund for Shanghai Talents, and the Program for Professor of Special Appointment (Eastern Scholar) at Shanghai Institutions of Higher Learning. Z.J. acknowledges the financial support from the National Natural Science Foundation of China (no. U1732267). XANES and EXAFS studies were carried out with the BL14W1 beamline at the Shanghai Synchrotron Radiation Facility (16ssrf00787). Z.-P.L. appreciates the support from National Key Research and Development Program of China (no. 2018YFA0208600). We thank Q. Liu from the University of Science and Technology of China for his helpful suggestions with synchrotron FTIR measurement and H. Zhang from the Shanghai Synchrotron Radiation Facility for his assistance in XPS analysis.

Author contributions

C.L., X.L. and J.-H.L. conceived the project design. C.L. prepared the samples and measured their electrochemical properties. C.L., S.-H.K., D.-H.K. and S.S.S. performed the XPS, SEM and TEM characterizations. S.Y., Y.Z., X.L. and Z.J. performed the operando measurements and analysed the data. J.-L.L., Y.-F.L. and Z.-P.L. performed the DFT calculations. C.L., X.L., Z.J. and J.-H.L. wrote and revised the paper with help from all authors. W.L. helped with the manuscript revision. J.-H.L. supervised the research.

Competing interests

The authors declare no competing interests.

Additional information

Supplementary information The online version contains supplementary material available at https://doi.org/10.1038/s41929-021-00703-0.

Correspondence and requests for materials should be addressed to Xiaopeng Li, Zhi-Pan Liu, Zheng Jiang or Jung-Ho Lee.

Peer review information *Nature Catalysis* thanks Sergio Rojas, Kirsten Winther and the other, anonymous, reviewer(s) for their contribution to the peer review of this work.

Reprints and permissions information is available at www.nature.com/reprints.

Publisher's note Springer Nature remains neutral with regard to jurisdictional claims in published maps and institutional affiliations.